

Chapter 7

Optical Corrals

Preface

The content that appears in this chapter has been largely adapted from the following publications:

McMahon JM, Gray SK, Schatz GC (2008) Dephasing of electromagnetic fields in scattering from an isolated slit in a gold film. Proc. SPIE 7033: 703311/1-6. doi: [10.1117/12.790647](https://doi.org/10.1117/12.790647)

Babayan Y, McMahon JM, Li S, Gray SK, Schatz GC, Odom TW (2009) Confining standing waves in optical corrals. ACS Nano 3:615–620. doi: [10.1021/nn8008596](https://doi.org/10.1021/nn8008596)

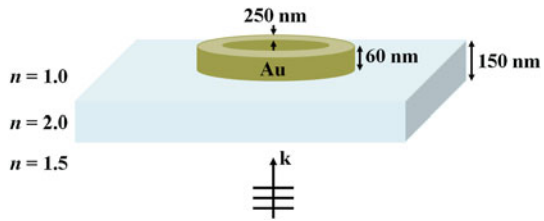
McMahon JM, Gray SK, Schatz GC (2011) Surface nanophotonics theory. In: Wiederrecht G (ed) Comprehensive Nanoscience and Technology. Elsevier, Amsterdam

The experimental work that appears in this chapter was done by Babayan Y and Odom TW. Although, the experimental aspects are not discussed heavily, and the reader interested in such details is referred to Refs. [1–3].

7.1 Introduction

In this chapter, FDTD modeling and near-field optical characterization of lithographically patterned arrays of micron-sized metallic circular rings are discussed, microscale (1–10 µm) analogues of the nanoscale quantum corral [4]. Such structures are of interest for confining and manipulating light on surfaces, which, for example, are of relevance for emerging applications in optoelectronics [5], photonics [5–7], and chemical and biological sensing [8, 9]. The wavelength dependence of such confinement will also be discussed. Additionally, elliptical corrals with three different eccentricities [$e = (1 - b^2/a^2)^{1/2}$, where a and b are the long and short axes, respectively] are discussed, which offer a novel platform

Fig. 7.1 Schematic diagram of an optical corral



for investigating polarization effects. Unlike in quantum corrals [4, 10, 11], such effects offer the potential to control the pattern of the standing waves. FDTD calculations of the intensities of the electric field $|E(x, \omega)|^2$ and magnetic field $|H(x, \omega)|^2$ are provided to support the experimental results. These calculations also reveal novel photonic effects, such as substrate effects and electromagnetic field dephasing, which are analyzed using a waveguide modal analysis. Such analysis is relevant for the aforementioned applications, but also enables a straightforward understanding of the relationship between NSOM measurements and the electric and magnetic fields that are typically used to interpret the corresponding near-field images.

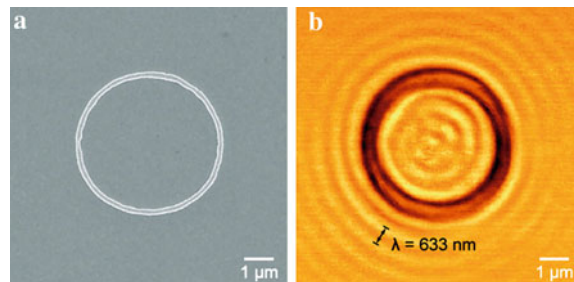
7.2 Computational Considerations

Isolated corrals were modeled after the experiments as 60 nm high (larger than the skin depth of Au at optical wavelengths of ~ 25 nm [12]) and 250 nm wide Au, Ag, or aluminum oxide (Al_2O_3) ring structures on top of a 150 nm thick $n = 2.0$ layer [similar to indium tin oxide (ITO)], and all on top of a glass ($n = 1.5$) substrate. A schematic diagram of the system under consideration is shown in Fig. 7.1. [2D FDTD calculations on analogous systems (not shown) indicate that isolated corrals produce results similar to those of a periodic array of them, such as the experimental ones in this chapter.] Computational domains were discretized using grid spacings of 5.0 nm in all directions. The dielectric functions of Au and Ag were modeled using the D2L model, accurately fit to empirically determined dielectric data over the relevant wavelengths (400–700 nm); Appendix B. Al_2O_3 was assumed to have a constant refractive index of $n = 1.77$. Field intensities were calculated 20 nm above the $n = 2.0$ layer by Fourier transforming the time-domain electric and magnetic fields.

7.3 Circular Corrals

Figure 7.2a shows a SEM image of a single circular corral made of Au with an inside diameter of 4.8 μm . When the structure is illuminated at normal incidence with circularly polarized 633 nm light and imaged by collection mode NSOM, two

Fig. 7.2 A circular optical corral. **a** SEM image of a $4.8\text{ }\mu\text{m}$ diameter Au corral, **b** NSOM image of **a** illuminated using circularly polarized 633 nm incident light



specific features are found inside and around the corral: (1) evanescent waves with $\sim 200\text{--}250\text{ nm}$ amplitude in the z -direction (normal to the surface), which can be quantified by single-point NSOM spectroscopy, and (2) standing wave patterns inside and outside of the structure with a wavelength close to that of the light used for imaging, as can be seen in Fig. 7.2b. The pattern inside the corral contains ripples, while that outside consists of concentric, circular fringes. In passing, it is interesting to note that the patterns formed within the optical corrals resemble the patterns of electronic standing waves in quantum corrals [4, 11, 10].

To investigate the effect of the corral size on the patterns, arrays of Au circular corrals with inner diameters of 2.23 and $5\text{ }\mu\text{m}$ center-to-center separations were fabricated; Fig. 7.3a. When these structures are imaged using circularly polarized 633 nm light, the number of internal ripples decrease (Fig. 7.3b, top), as expected, and the central spots become dark. These results are similar to those observed in NSOM images of the local density of states inside $2.7\text{-}\mu\text{m}$ circular Au discrete-wall corrals [13]. In addition, the standing wave pattern outside of the corrals becomes more well-defined. FDTD calculations of $|E(x, \omega)|^2$ for a $2.23\text{-}\mu\text{m}$ circular Au corral shows good agreement with the experimental patterns both inside and around the corral, including the peak-to-peak wavelength of the standing waves and the positions of the maxima and minima; Fig. 7.3c.

Changes in the intensity and pattern of the standing waves outside of the corrals can easily be explained as diffraction between opposite corral walls from both individual and neighboring corrals, where the longer wavelengths correspond to lower diffraction orders, and are thus more intense. However, the fields inside the corrals are found to only depend on the geometry and local dielectric environment of an individual corral. For example, calculations without the ITO substrate produces significantly different field patterns; Fig. 7.4. Without the substrate, the trends of the maxima and minima are reversed compared to its inclusion, and also resemble slit waveguide modes excited with TE_z polarized light [2]; see Sect. 7.4. These results demonstrate that the confined fields in the optical corrals can be tuned by the changing the substrate. The primary reason for this is that the effective incident wavelength in the corrals depends on the substrate, $\lambda_{\text{eff}} = \lambda_0/\epsilon_{\text{sub}}^{1/2}$, where λ_{eff} is the effective incident wavelength and λ_0 is the actual incident wavelength inside the substrate with permittivity ϵ_{sub} . Presumably, the field

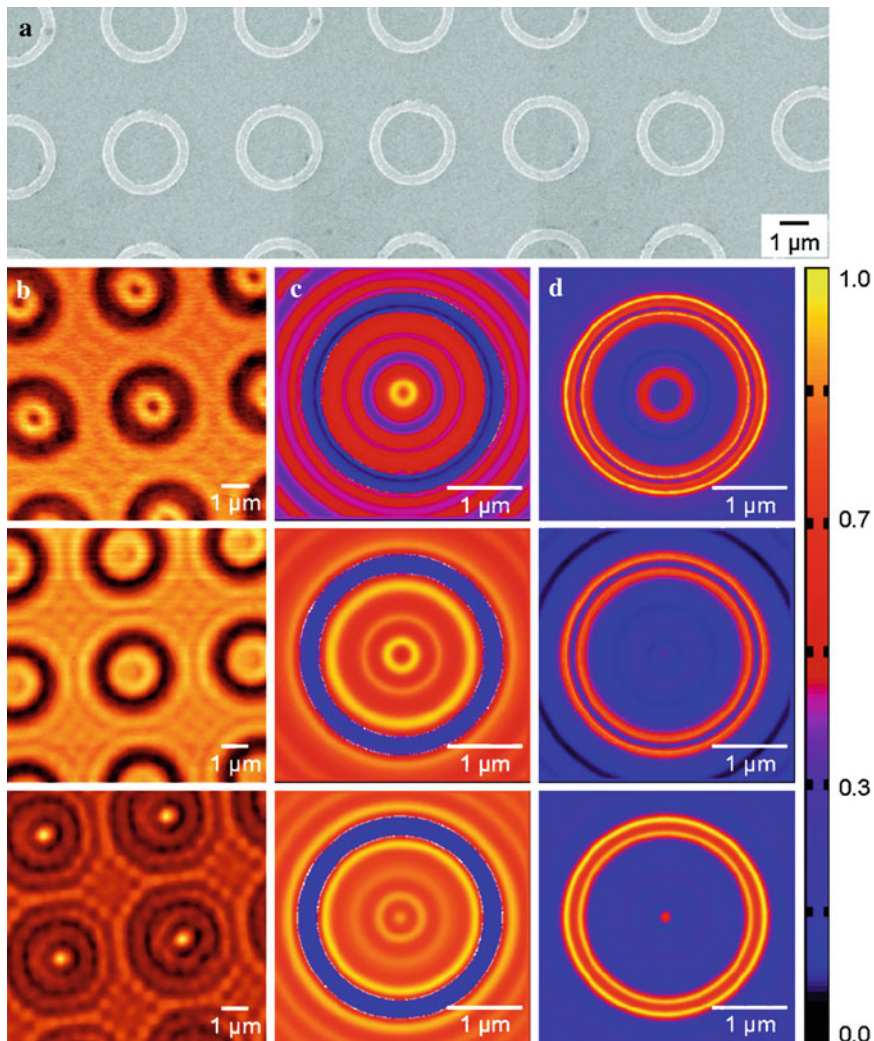


Fig. 7.3 Wavelength dependence of standing wave patterns in circular corrals. **a** SEM image of arrays of $2.23\text{ }\mu\text{m}$ diameter Au corrals, **b** Collection mode NSOM images of the corrals under *top* 633, *middle* 543, and *bottom* 457-nm light. FDTD calculations of **c** $|E(x, \omega)|^2$ and **d** $|H(x, \omega)|^2$ for the same conditions as in **b**

patterns will be completely reversed when $d(1 - \epsilon_{\text{sub}}^{1/2})/\lambda_0 = n + 1/2$, where $n = 0, 1, 2, \dots$ and d is the corral diameter.

Interestingly, $|E(x, \omega)|^2$ and $|H(x, \omega)|^2$ are found to be qualitatively backwards within the corrals; Figs. 7.3c, d and 7.4. This feature can be explained by performing calculations on a simplified system and using a waveguide modal analysis [2, 14]; see Sect. 7.4.

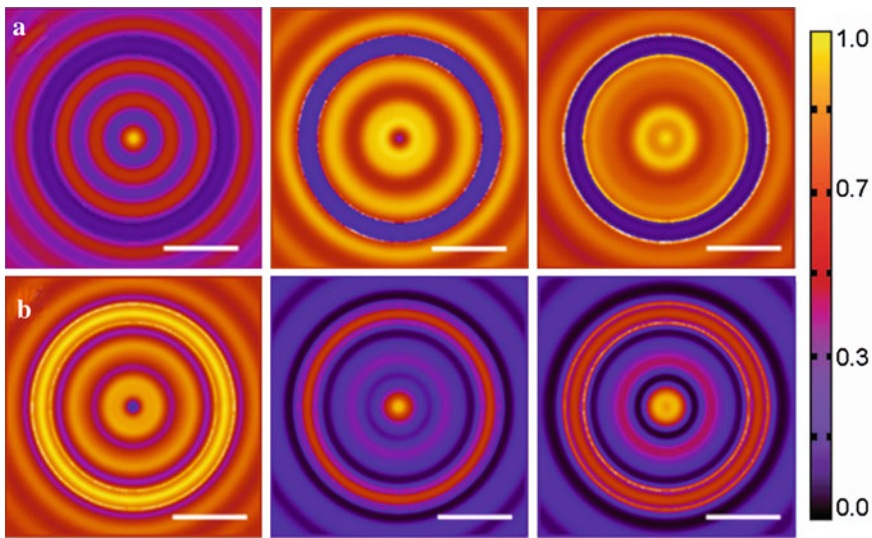


Fig. 7.4 FDTD calculated **a** $|E(x, \omega)|^2$ and **b** $|H(x, \omega)|^2$ inside a $2.23\text{ }\mu\text{m}$ inner diameter circular Au corral with no substrate for *left* 457, *middle* 543, and *right* 633 nm incident light. Scale bars represent $1\text{ }\mu\text{m}$

Variations of the standing wave patterns in response to a change in the wavelength of the light are also observed. The $2.23\text{-}\mu\text{m}$ corrals illuminated and imaged using two additional wavelengths, 543 and 457 nm, are shown in Fig. 7.3b, c *middle* and *bottom*. When the 633-nm light is replaced with 543-nm, and then with 457-nm, the dark spot in the middle of the corral gradually switches to a bright one (Fig. 7.3b, *bottom*), which has an intensity ~ 6 times higher than the lowest intensity spot. This observation suggests that only certain wavelengths of light are optimally sustained inside the corrals to produce a high intensity spot at the center.

To investigate the effect of the corral material on the patterns, circular corrals with Ag and Al_2O_3 (dielectric) walls with inner diameters of $2.35\text{ }\mu\text{m}$ were also fabricated; Fig. 7.5. When the corrals are excited with circularly polarized 633-nm light, identical patterns are produced inside both the metallic and dielectric structures, Fig. 7.5a, b, respectively. The dielectric corrals, however, are brighter than the metallic ones, which is expected because Al_2O_3 is transparent. Another variation between the images is in the contrast of the standing wave patterns, which indicates that the reflectivity of the corral material is important (a result not necessarily expected, *a priori*). Based on reflectivity values, the dielectric structures have the lowest contrast because that of Al_2O_3 is lower, compared to the metals, at 633 nm. Between the two metals, Ag has a slightly better contrast because it has $\sim 5\%$ higher reflectivity at 633 nm than Au [15]. FDTD calculations of $|E(x, \omega)|^2$ for these corrals again support the experimentally observed results; Fig. 7.5, *right*.

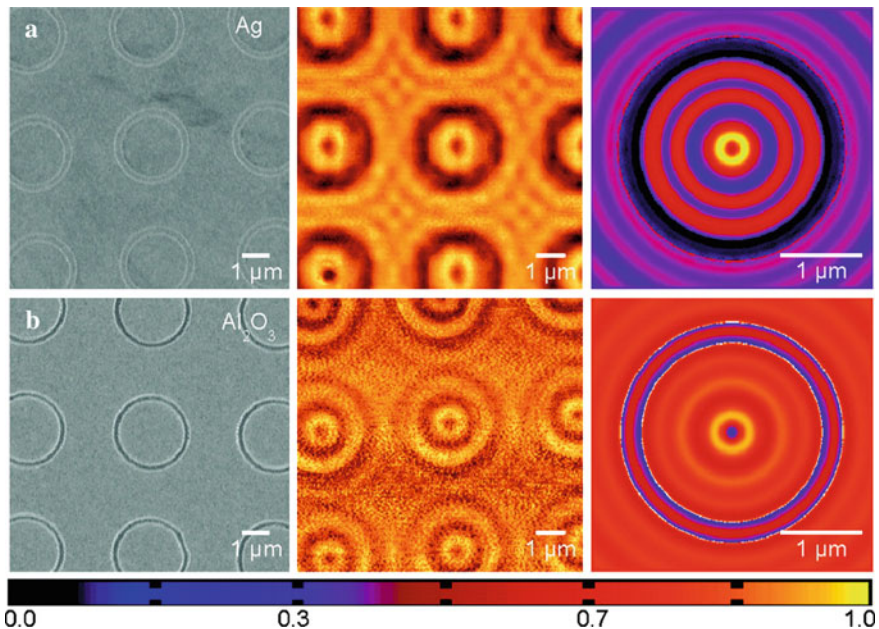


Fig. 7.5 Corral material dependence of standing wave patterns. *left* SEM, *middle* NSOM, and *right* FDTD calculations of $|E(x, \omega)|^2$ for **a** Ag and **b** Al_2O_3 corrals illuminated using 633-nm light

7.4 1D Corrals (Isolated Slits)

In order to understand the results in Sect. 7.3, it is helpful to focus on a simplified structure, a 1D slit with a width (d) of the same diameter as the corrals ($d = 2.23 \mu\text{m}$) in a thin Au film (also with thickness of $h = 60 \text{ nm}$) in air. In this way, the behavior of confined EM fields for 543-nm TE_z , TM_z , and circular (which contains both TE_z and TM_z polarizations, but out of phase) incident polarizations of light can be determined (polarizations which can all be important in the full structures). Figure 3.10 shows a schematic diagram of the system under consideration for TE_z polarization.

$|E(x, \omega)|^2$ and $|H(x, \omega)|^2$ inside the slit calculated with FDTD for TE_z polarization are shown in Fig. 7.6a. It is seen that the fields have oscillatory behavior within the slit, with a peak-to-peak separation of 515 and 545 nm for $|E(x, \omega)|^2$ and $|H(x, \omega)|^2$, respectively, which is very close to the free-space wavelength of 543 nm. In addition, it is seen that $|E(x, \omega)|^2$ and $|H(x, \omega)|^2$ are backwards. Both trends agree very well with the results in Sect. 7.3 for the full corral systems.

Assuming that Au can be treated as a PEC, the transverse component of the field inside the slit can be expanded as a superposition of the eigenmodes of a 1D parallel-plate waveguide, and a modal analysis can be used to gain physical insight into the problem [1, 2]; see Sect. 3.5.2. The field intensities calculated with this

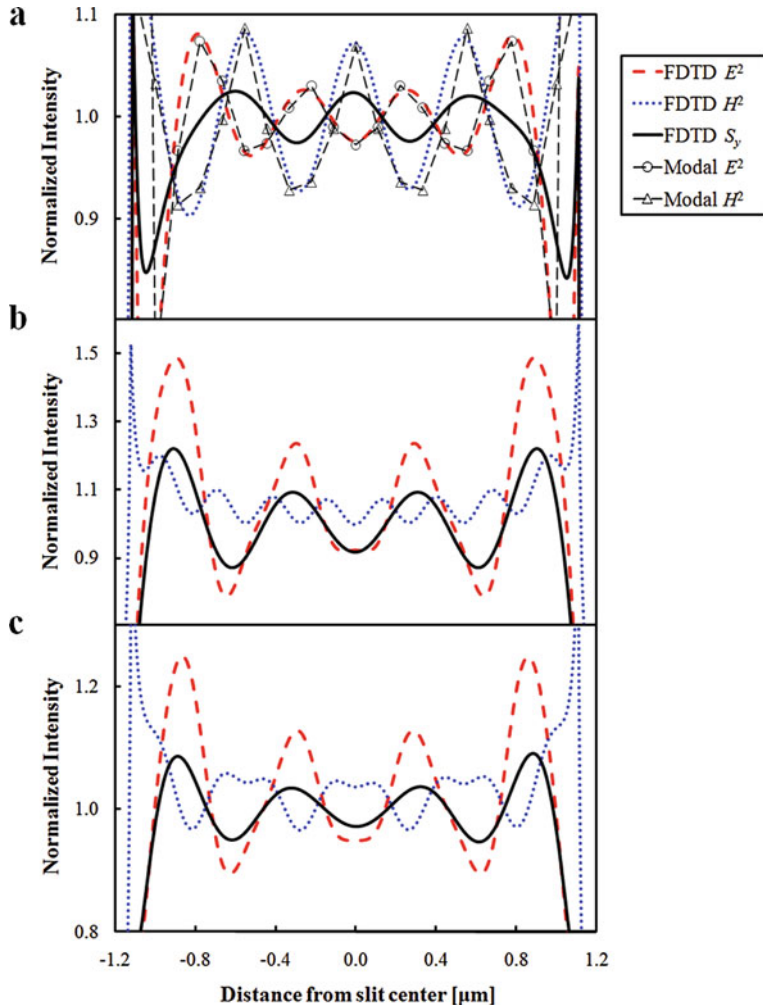
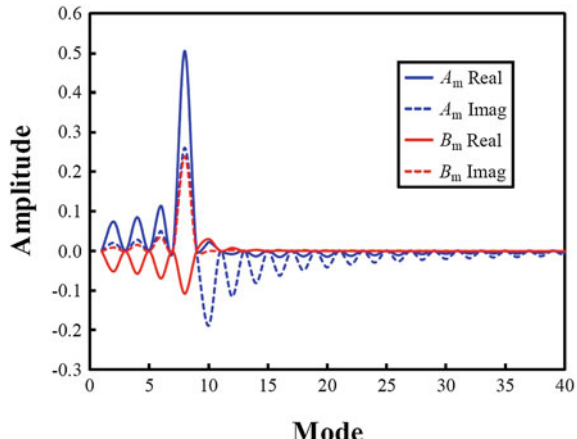


Fig. 7.6 FDTD calculated field intensities inside and power flow through a $d = 2.23 \mu\text{m}$ diameter slit in a $h = 60 \text{ nm}$ thick Au film for 543-nm incident light **a** TE_z , **b** TM_z , and **c** circularly polarized. Modal expansion method results are also shown for a PEC film for TE_z polarization

method are shown in Fig. 7.6a. The results agree very well with the FDTD calculations, confirming that the behavior of the fields inside a slit in a Au film and a PEC are similar.

The amplitudes of the waveguide modes, A_m and B_m in Eq. 3.111, obtained from the modal analysis are shown in Fig. 7.7. It is seen that coefficients are mainly composed of the $m = 0$ and $m = 8$ modes. The latter mode is entirely imaginary, which means that scattering by the slit (corral) induces a modal transition from propagating to evanescent. The transitional evanescent mode

Fig. 7.7 Amplitudes of the waveguide modes inside a $d = 2.23 \mu\text{m}$ diameter slit in a $h = 60 \text{ nm}$ thick PEC film for 543-nm TE_z polarized incident light. The $m = 0$ mode, which has amplitudes of $A_m = 0.658 - i0.846$ and $B_m = 0.601 + i0.858$, is not shown for clarity



corresponds to light that propagates parallel to the surface with a wavelength just slightly shorter than the incident light ($m\pi/d \approx k_0\epsilon_s^{1/2}$). This analysis thus explains the similarity between this wavelength and the peak-to-peak separation of the standing waves, as well as their evanescent character. Furthermore, the superposition of the high-order evanescent modes onto the propagating ones explains the backwards behavior between $|E(x, \omega)|^2$ and $|H(x, \omega)|^2$. Lastly, this analysis explains the corral material dependence results, as $\phi_m(x)$ in the modal analysis (Sect. 3.5.2) (and the equivalent expression for TM_z polarization) is better satisfied as the reflectivity (or equivalently, the dielectric constant) goes to infinity. As this happens, the intensity of the confined waves should (and does) become stronger.

FDTD calculations of the normal component of the Poynting vector (a measure of the power flow), S_y , inside the slit are also shown in Fig. 7.6a. It is seen that power flow through the slit is governed by $|H(x, \omega)|^2$, except near the slit edges.

To completely describe all aspects of the full systems, other polarizations (e.g., TM_z polarization) need to be taken into account. The values of $|E(x, \omega)|^2$, $|H(x, \omega)|^2$, and S_y calculated using FDTD for TM_z polarization are shown in Fig. 7.6b. It is seen that the peak-to-peak separation of $|E(x, \omega)|^2$ is 590 nm, which again is very close to the free-space wavelength of 543 nm. However, the peak-to-peak separation of $|H(x, \omega)|^2$ is 270 nm, close to half of the free-space wavelength. This can be attributed to $H(x, \omega)$ components composed almost entirely of the $m = 8$ waveguide mode. This result is also seen for the y -component of $E(x, \omega)$ for TE_z polarization (not shown), except that it is overshadowed by the x -component, which contains both $m = 0$ and $m = 8$ modes. Additionally, for TM_z polarization, the power flow throughout the entire slit is governed by $E(x, \omega)$.

Finally, properties of $|E(x, \omega)|^2$, $|H(x, \omega)|^2$, and S_y calculated using FDTD for circular polarization are shown in Fig. 7.6c. The results are essentially a superposition of the TE_z and TM_z polarized results. However, the power flow throughout the entire slit is governed by $E(x, \omega)$, similar to the TM_z polarization results.

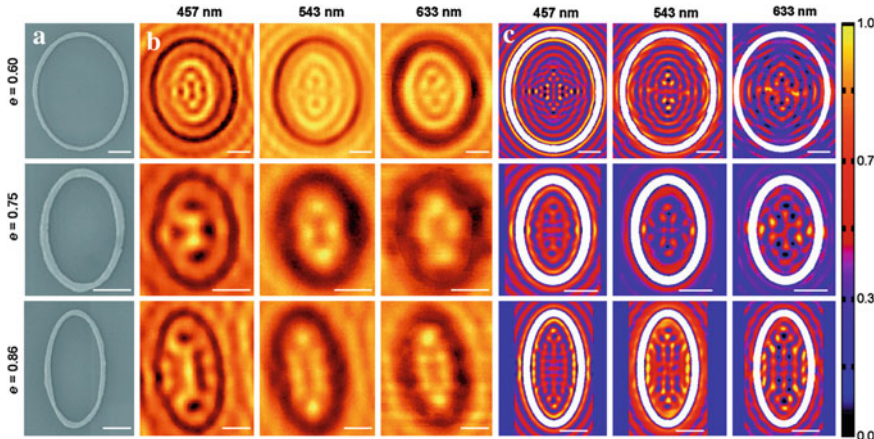


Fig. 7.8 Effect of the ellipse shape on the pattern of standing waves. **a** SEM images of ellipses with eccentricities of $e = \text{top } 0.60, \text{middle } 0.75, \text{and bottom } 0.86$. **b** NSOM images for the corrals in **a** under circularly polarized light. **c** FDTD calculations of $|E(x, \omega)|^2$ for the corrals in **a**. All scale bars represent $1 \mu\text{m}$

7.5 Elliptical Corrals

Although circular corrals provide a simple platform for studying the optical analogue of the quantum corral, more complex structures provide additional ways to manipulate light on dielectric surfaces. For example, structures with lower symmetries provide unique opportunities to study polarization effects on light confinement within the corral structures. Figure 7.8a shows ellipses with eccentricities of $e = 0.60$ ($a = 2.5 \mu\text{m}$, $b = 2 \mu\text{m}$), $e = 0.86$ ($a = 2 \mu\text{m}$, $b = 1 \mu\text{m}$), and $e = 0.75$ ($a = 1.5 \mu\text{m}$, $b = 1 \mu\text{m}$). Upon illumination of the ellipses with circularly polarized 457-nm light, complex patterns, which resemble those of quantum corrals with similar eccentricities [10], are formed inside the structures; Fig. 7.8b. Interestingly, ellipses with $e = 0.75$ and 0.86 suppress light at their focal points (dark spots are present), while the $e = 0.60$ ellipse does not. To investigate whether this phenomenon is related to the structure of the corral or to the wavelength of light used for imaging, ellipses imaged with 543 and 633-nm light are shown in Fig. 7.8b as well. For these wavelengths, the ellipses with larger eccentricities show bright spots at their focal points. These results demonstrate that the standing wave patterns can be controlled by changing either the shape of the corral or the excitation wavelength of light.

FDTD calculations were carried out for the elliptical corrals excited with circularly polarized light, and are shown in Fig. 7.8c. As with the circular corrals, $|E(x, \omega)|^2$ agrees well with experiment, and $|E(x, \omega)|^2$ and $|H(x, \omega)|^2$ are

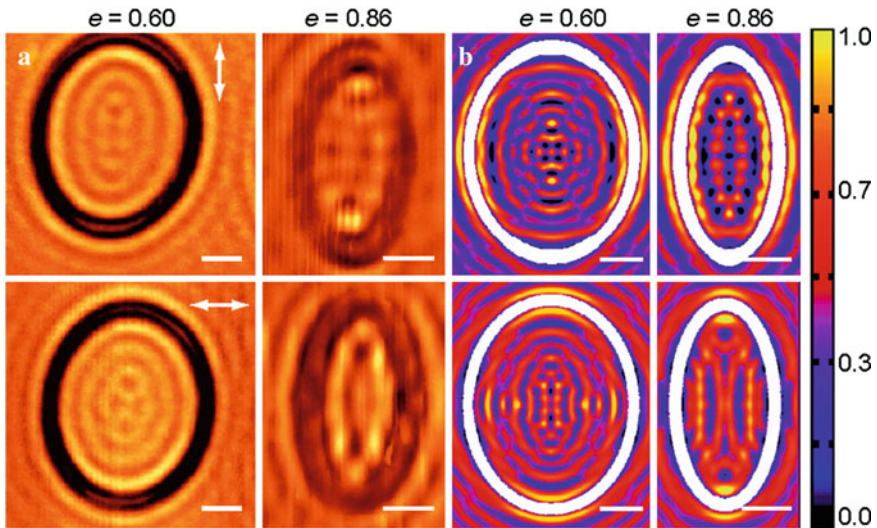


Fig. 7.9 Polarization effects on standing-wave patterns. **a** Ellipses with $e = 0.60$ and 0.86 imaged using 543-nm light with $E(x, \omega)$ linearly polarized along either the *top* long or *bottom* short axis. **b** FDTD calculations of $|E(x, \omega)|^2$. In **b**, the ellipses are outlined in white; all scale bars represent $1\text{ }\mu\text{m}$

backwards (not shown). Based on the discussion in Sect. 7.4, all of these results can be understood as arising from interference between waveguide modes that are excited by the short and long axes of the corrals, which also dephases the fields.

Because of the low symmetries of the elliptical corrals, the fields confined within them are expected to exhibit a polarization dependence. The $e = 0.60$ and 0.86 ellipses imaged using linearly polarized (along either the short or long axis) 543-nm light are shown in Fig. 7.9a. FDTD calculations were also carried out for the elliptical corrals excited with linearly polarized light, and support the experimentally observed trends; Fig. 7.9b. These results confirm that standing wave patterns can be tailored by simply changing the polarization direction of the incident light, and once again can be explained using the same analysis given in Sect. 7.4. In the elliptical corrals, however, an asymmetric excitation of TE_z and TM_z polarized waveguide modes occurs, and the FDTD results show that the TM_z polarized waveguide mode is dominant.

7.6 Summary

A study of corral structures was presented. Such structures were shown to be useful to confine and manipulate light on dielectric surfaces, and can be considered optical analogues to quantum corrals. Circular corrals were used to elucidate the

basic effects in such structures, such as well-defined standing wave patterns. Such effects were shown to exhibit corral size, wavelength, material, and substrate dependencies. FDTD calculations supported the experimental results, and also revealed that $|E(x, \omega)|^2$ matches the measurements, while $|H(x, \omega)|^2$ is backwards.

In order to explain these effects, a simple waveguide model was used. These results helped determine that light scattering from the corrals produces evanescent waveguide modes at the dielectric interface with an effective wavelength similar to that of the incident light. Furthermore, when these modes are superimposed onto the propagating ones, a dephasing of $|E(x, \omega)|^2$ and $|H(x, \omega)|^2$ occurs. The results in Fig. 7.6 are particularly important to the interpretation of NSOM imaging measurements, as they show that the power flow (which is the property that is directly probed) provides a measurement of the local $E(x, \omega)$ in some cases and the local $H(x, \omega)$ in others. While this can complicate the use of NSOM to experimentally study interference effects, FDTD and the modal expansion method provide simple ways to model the results.

The aforementioned effects were further investigated in elliptical structures, which offer further tunability of the standing-wave patterns through both their eccentricity and the polarization of the incident light.

References

1. Babayan Y, McMahon JM, Li S, Gray SK, Schatz GC, Odom TW (2009) Confining standing waves in optical corrals. *ACS Nano* 3:615–620
2. McMahon JM, Gray SK, Schatz GC (2008) Dephasing of electromagnetic fields in scattering from an isolated slit in a gold film. In: Kawata S (ed), *Plasmonics: Nanoimaging, Nanofabrication, and Their Applications IV* 703311-1–6
3. McMahon JM, Gray SK, Schatz GC (2011) Surface nanophotonics theory. In: Wiederrecht G (ed) *Comprehensive Nanoscience and Technology*. Elsevier, Amsterdam
4. Crommie MF, Lutz CP, Eigler DM (1993) Confinement of electrons to quantum corrals on a metal surface. *Science* 262:218–220
5. Barnes WL, Dereux A, Ebbesen TW (2003) Surface plasmon subwavelength optics. *Nature* 424:824–830
6. Ebbesen TW, Lezec HJ, Ghaemi HF, Thio T, Wolff PA (1998) Extraordinary optical transmission through subwavelength hole arrays. *Nature* 391:667–669
7. Ozbay E (2006) Plasmonics: Merging photonics and electronics at nanoscale dimensions. *Science* 311:189–193
8. Haes AJ, Haynes CL, McFarland AD, Schatz GC, Van Duyne RP, Zou S (2005) Plasmonic materials for surface-enhanced sensing and spectroscopy. *MRS Bull* 30:368–375
9. Willets KA, Van Duyne RP (2007) Localized surface plasmon resonance spectroscopy and sensing. *Annu Rev Phys Chem* 58:267–297
10. Fiete GA, Heller EJ (2003) Colloquium: Theory of quantum corrals and quantum mirages. *Rev Mod Phys* 75:933–948
11. Manoharan HC, Lutz CP, Eigler DM (2000) Quantum mirages formed by coherent projection of electronic structure. *Nature* 403:512–515
12. Dawson P, Boyle MG (2006) Light emission from scanning tunneling microscope on polycrystalline Au films: What is happening at the single-grain level? *J Opt A-Pure Appl Opt* 8:S219–S226

13. Dereux A, Girard C, Chicanne C, Colasdes Francs G, David T, Bourillot E, Lacroute Y, Weeber JC (2003) Subwavelength mapping of surface photonic states. *Nanotechnology* 14:935–938
14. Bravo-Abad J, Martín-Moreno L, García-Vidal FJ (2004) Transmission properties of a single metallic slit: From the subwavelength regime to the geometrical-optics limit. *Phys Rev E* 69:026601
15. Johnson PB, Christy RW (1972) Optical constants of the noble metals. *Phys Rev B* 6:4370–4379